Atmos. Meas. Tech., 17, 3085–3101, 2024
https://doi.org/10.5194/amt-17-3085-2024

Atmospheric Measurement Techniques
Open Access
EGU

Multi-wavelength dataset of aerosol extinction profiles retrieved from GOMOS stellar occultation measurements

Viktoria F. Sofieva[1], Monika Szelag[1], Johanna Tamminen[1], Didier Fussen[2], Christine Bingen[2], Filip Vanhellemont[2], Nina Mateshvili[2], Alexei Rozanov[3], and Christine Pohl[3]

[1]Finnish Meteorological Institute, Helsinki, Finland
[2]Royal Belgian Institute for Space Aeronomy (BIRA-IASB), Brussels, Belgium
[3]Institute of Environmental Physics, University of Bremen, Bremen, Germany

Correspondence: Viktoria F. Sofieva (viktoria.sofieva@fmi.fi)

Received: 14 August 2023 – Discussion started: 21 August 2023
Revised: 18 March 2024 – Accepted: 18 March 2024 – Published: 23 May 2024

Abstract. In this paper, we present the new multi-wavelength dataset of aerosol extinction profiles, which are retrieved from the averaged transmittance spectra by the Global Ozone Monitoring by Occultation of Stars instrument aboard the Envisat satellite.

Using monthly and zonally averaged transmittances as a starting point for the retrievals enables us to improve the signal-to-noise ratio and eliminate possible modulation of transmittance spectra by uncorrected scintillations. The two-step retrieval method is used: the spectral inversion is followed by the vertical inversion. The spectral inversion relies on the removal of contributions from ozone, NO_2, NO_3 and Rayleigh scattering from the optical depth spectra for each ray perigee altitude. In the vertical inversion, the profiles of aerosol extinction coefficients at several wavelengths are retrieved from the collection of slant aerosol optical depth profiles.

The retrieved aerosol extinction profiles (FMI-GOMOSaero dataset v1) are provided in the altitude range 10–40 km at wavelengths of 400, 440, 452, 470, 500, 525, 550, 672 and 750 nm for the whole GOMOS operating period from August 2002 to March 2012.

Extensive intercomparisons of the retrieved FMI-GOMOSaero aerosol profiles with aerosol profile data from other satellite instruments at several wavelengths have been performed. It is found that the average difference between FMI-GOMOSaero and other datasets is within 20 %–40 % in the lower and middle stratosphere, the standard deviation is ∼ 20 %–50 %, and the correlation coefficient of the time series is 0.65–0.85.

The created FMI-GOMOSaero dataset can be used in merged datasets of stratospheric aerosols. It might be also used as a priori information for satellite retrievals during 2002–2012.

1 Introduction

Stratospheric aerosols impact the radiative forcing and thus the energy balance of the Earth's atmosphere; therefore, information about their distribution and variability is of high importance for climate-related studies. The stellar occultation instrument GOMOS (Global Ozone Monitoring by Occultation of Stars), which operated on the Envisat satellite during 2002–2012, was capable of providing the profiles of aerosol extinction coefficient in the altitude range from ∼ 10 to 40 km (Kyrölä et al., 2010; Bertaux et al., 2010; Vanhellemont et al., 2010). The GOMOS aerosol data have already been used in the merged stratospheric aerosol dataset (Vernier et al., 2011) and climate studies (Solomon et al., 2011; Santer et al., 2014; Brühl et al., 2018; Schallock et al., 2023), as well as to produce reference climate data records (Popp et al., 2016; Bingen et al., 2017).

GOMOS was equipped with UV–VIS (250–690 nm) and IR (755–774 and 926–954 nm) grating spectrometers operating at a sampling frequency of 2 Hz, with two fast photometers at ∼ 472 nm and ∼ 672 nm operating at 1 kHz sampling frequency. GOMOS measured stellar irradiance in the limb-viewing geometry from ∼ 140 km down to full extinction at about 10–15 km (Bertaux et al., 2010). The transmit-

tance spectra are obtained after dividing the stellar spectra observed through the atmosphere by the reference spectrum above the atmosphere. After correction of refraction effects (refractive attenuation and scintillation), the transmittance spectra are the basis for retrievals of trace gases and aerosol extinction.

The GOMOS IPF (Instrument Processor Facility) v6 retrievals of ozone, NO_2, NO_3 and aerosol extinction rely on a two-step inversion (Kyrölä et al., 2010). First, the horizontal column densities are retrieved from transmittance spectra $T(\lambda, z)$ for each tangent altitude (the spectral inversion). After that, the local density profiles are obtained from the profiles of horizontal column densities (the vertical inversion). In the IPF spectral inversion, the contribution due to Rayleigh scattering is estimated using the ECMWF data, and horizontal column densities of ozone, NO_2, NO_3 and aerosol extinction are retrieved simultaneously from UV–VIS spectrometer data, with iterative DOAS-type[1] inversion for NO_2 and NO_3. Since the spectral dependence of aerosol cross-sections, which depend on particle size distribution, is not known, the IPF v6 processor uses a parameterization via a second-degree polynomial model in wavelength λ (Kyrölä et al., 2010; Vanhellemont et al., 2010). The GOMOS IPF v6 processor provides the aerosol extinction coefficient data record at 500 nm and its spectral dependence, expressed by the coefficients of the polynomial mentioned above.

In the AERGOM processor, which is optimized for aerosol retrievals (Vanhellemont et al., 2016), the data from the spectrometer B1 (755–774 nm) are also used together with the UV–VIS spectrometer data for retrievals of aerosol extinction. In AERGOM, the spectral dependence of aerosol extinction is parameterized by a second-degree polynomial in $1/\lambda$. As in IPF v6, the retrievals are performed in two steps: the non-linear spectral inversion is followed by the linear vertical inversion. In the AERGOM spectral inversion, horizontal column densities of ozone, NO_2, NO_3 and aerosol extinction are retrieved simultaneously from UV–VIS spectrometer data. Covariances between species after the spectral inversion are taken into account in AERGOM, while they are neglected in the IPF v6 processor. AERGOM performs the vertical inversion for all species simultaneously, while the IPF v6 processor does it for each species separately, with a decreased information content. Finally, for aerosol extinction, AERGOM applies three altitudinal regularization constraints (at three wavelengths), while IPF v6 applies only one (aerosol extinction at 500 nm). From all AERGOM vertical aerosol extinction coefficient profiles, a 5 d gridded climate data record with a spatial resolution of 5° latitude and 60° longitude was created (Bingen et al., 2017). This climate data record, which is referred to as CCI-AERGOM and is available at https://cds.climate.copernicus.eu/cdsapp#!/dataset/10.24381/cds.239d815c?tab=form (last access: 5 May 2024), contains the profiles of average aerosol extinction coefficient at 355, 440, 470, 550 and 750 nm.

Although GOMOS aerosol extinction coefficient data are available from the ESA IPF v6 and AERGOM processors, the reported spectral dependence of the aerosol extinction is often not realistic, mainly due to interference with ozone retrievals, limited wavelength range in the IPF v6 retrievals, insufficient signal-to-noise ratio, residual scintillation and the limitations of the polynomial model. In particular, it is known that lower-stratospheric ozone in IPF v6 has a strong bias, and this influences the quality of aerosol retrievals, as ozone and aerosols are retrieved simultaneously. The AERGOM aerosol extinction was reported to show a negative bias above 25 km altitude for wavelengths larger than 700 nm (Robert et al., 2016).

In this paper, we aim at addressing these issues by using averaged GOMOS transmissions to create a multi-wavelength aerosol extinction profile dataset (climate data record). The proposed new algorithm for aerosol retrievals is based on the removal of extinctions due to the Rayleigh scattering and absorption by ozone and other trace gases from monthly and zonally averaged GOMOS transmission spectra. We aim at creating a reliable GOMOS dataset of stratospheric aerosols, which can be included in climate data records.

The paper is organized as follows. Section 2 describes the inversion algorithm. The retrieval results and various intercomparisons are presented in Sect. 3. Section 4 is dedicated to characterization of the entire retrieved GOMOS aerosol dataset as a climate data record. The Summary section (Sect. 5) concludes the paper.

2 The inversion algorithm

2.1 Preparation for retrievals: creating the averaged transmittances dataset

The monthly averaged transmittances as a function of wavelength λ and tangent altitude z, $T(\lambda, z)$, are used as a starting point for the retrievals. The self-calibrating property of the occultation method suggests averaging of independent observations for the sake of augmenting their statistical significance. This technique allows for the detection of very weak absorbers (e.g., OClO, Fussen et al., 2006, or Na, Fussen et al., 2010), as it increases the signal-to-noise ratio. Furthermore, the level of the stochastic residual scintillations is greatly reduced.

For computing averaged transmittances, we used GOMOS nighttime measurements (i.e., with a solar zenith angle at the ray perigee point larger than 107°). The refractive effects – refractive dilution and perturbations due to scintillations – are estimated and removed from the transmittance spectra for each occultation (Dalaudier et al., 2001; Sofieva et al., 2009; Kyrölä et al., 2010). The transmittances with removed

[1] Differential optical absorption spectroscopy.

refractive effects (EXT product) are used in our computations. In order to ensure a sufficient number of occultations, 10° latitude zones are selected for averaging. The methodology for computing the GOMOS averaged transmittances has been developed in the dedicated ESA project ALGOM (https://earth.esa.int/eogateway/activities/algom, last access: 4 May 2024). It includes interpolation of transmittances at a fixed altitude grid, outlier filtering and data averaging. Because of the noise specifics, GOMOS data have outliers, which affect 2 %–4 % of dark-limb occultations (Bertaux et al., 2010; https://earth.esa.int/eogateway/documents/20142/37627/GOMOS-Level-2-processor-version-GOMOS-6.01-Readme.pdf, last access: 4 May 2024). The outlier filtering is performed using an algorithm based on the well-known jackknife method (e.g., Miller, 1974). The threshold for outliers has been chosen as 3 standard deviations from the median.

For each tangent altitude and each wavelength, the average transmittance is computed as the weighted median transmittance. This estimate is insensitive to outliers, and it takes into account the signal-to-noise ratio of different measurements, which can differ considerably for GOMOS due to different stellar sources. The transmittances are weighted with respect to the inverse of their estimated measurement errors. A classical definition of the weighted median was used (Edgeworth, 1888). Technically, it was computed as a central element of a sorted set, in which values are replicated according to their relative weights. A potential drawback of using a median instead of a mean is that it may potentially exclude isolated events such as pyrocumulonimbus events or the early stages of a volcanic eruption (note that local signals are also diluted by spatiotemporal averaging).

The examples of averaged transmittances for the latitude bin 0–10° N are shown in Fig. 1 for conditions of a low loading level (January 2003, Fig. 1a) and increased aerosols after Soufrière Hills and Rabaul volcanic eruptions (January 2007, Fig. 1b). It is clearly seen that the transmittances are lower (optical depth is higher) for the volcanic aerosol conditions (e.g., compare transmittances at 20 km, which are highlighted by thick red lines).

2.2 Aerosol retrieval algorithm

The idea of aerosol retrievals from averaged transmittances with removed refractive effects is very simple. If the extinction due to Rayleigh scattering and due to absorption by ozone, NO_2 and NO_3 can be removed from the GOMOS extinction spectra, the remaining part is due to aerosol extinction.

The GOMOS spectral inversion

$$T = \exp\left(-\left(\tau_{O_3} + \tau_{NO_2} + \tau_{NO_3} + \tau_{air} + \tau_{aero}\right)\right) + \epsilon, \qquad (1)$$

where τ_{O_3}, τ_{NO_2}, τ_{NO_3}, τ_{air} and τ_{aero} are contributions to the optical depth due to ozone, NO_2, NO_3, Rayleigh scattering and aerosols, respectively, and ϵ is noise, is weakly nonlinear. It can be linearized by simply taking the logarithm. Provided the measurement noise is low, a Gaussian approximation of the noise distribution for the linearized problem still holds. The GOMOS spectral inversion, its linearization and associated distribution of noise are discussed in detail in Kyrölä et al. (1993), Tamminen and Kyrölä (2001), and Tamminen (2004).

We used data from spectrometer A at wavelengths 380–672 nm and spectrometer B1 at wavelengths 755–759 nm. The NO_2 and NO_3 optical depths are computed using retrieved GOMOS NO_2 and NO_3 profiles, which are averaged in the corresponding month and latitude bin (Alternatively, NO_2 and NO_3 can be directly retrieved from the averaged transmittances. Since the NO_2 and NO_3 retrievals are not the subject for this study and since the standard GOMOS DOAS-type retrieval provides good-quality NO_2 and NO_3, we use them for the aerosol retrievals.) The Rayleigh extinction is computed using ECMWF air density data provided in the GOMOS files, which are averaged in the same way. As in ALGOM2S retrievals (Sofieva et al., 2017), ozone optical depth is computed using a DOAS-type retrieval with the triplet in the Chappuis band (reference wavelengths are 523–527 and 673–677 nm; absorbing wavelengths are 598–602 nm). In the processing, we filtered out unreliable averaged transmittance values (with estimated uncertainties exceeding 100 %).

The details of the retrieval of horizontal aerosol optical depth are illustrated in Fig. 2 for the altitude of 20 km near the Equator (0–10° S). The measured total optical depth, $\tau(\lambda, z) = -\log(T)$, is shown by the black line. The estimated optical depths due to ozone (τ_{ozone}), $NO_2(\tau_{NO_2})$, $NO_3(\tau_{NO_3})$ and Rayleigh extinction (τ_{air}) are shown by colored lines in the upper panel of Fig. 2.

The resulting residuals,

$$R(\lambda, z) = \tau(\lambda, z) - \tau_{ozone}(\lambda, z) - \tau_{air}(\lambda, z) - \tau_{NO_2}(\lambda, z) - \tau_{NO_3}(\lambda, z), \qquad (2)$$

are due to aerosols. The residual spectra are smoothed and sampled at nine wavelengths (400, 440, 452, 470, 500, 525, 550, 672 and 750 nm), resulting in the horizontal aerosol optical depth spectra $\tau_{aero}(\lambda, z)$ at each tangent altitude. The wavelengths are selected to be as used by other instruments/retrievals.

In the vertical inversion, the profiles of local aerosol extinction coefficients are reconstructed from the horizontal aerosol optical depth profiles $\tau_{aero}(\lambda, z)$ for each wavelength. The GOMOS vertical inversion is linear, and it is performed in the same way as in the GOMOS processor (Kyrölä et al., 2010). The target-resolution Tikhonov-type regularization is applied in the vertical inversion (Sofieva et al., 2004; Kyrölä et al., 2010). The resulting actual altitude resolution of the aerosol extinction profiles $\beta(\lambda, z)$ is 3 km. The uncertainties of retrieved aerosol extinction profiles are estimated via er-

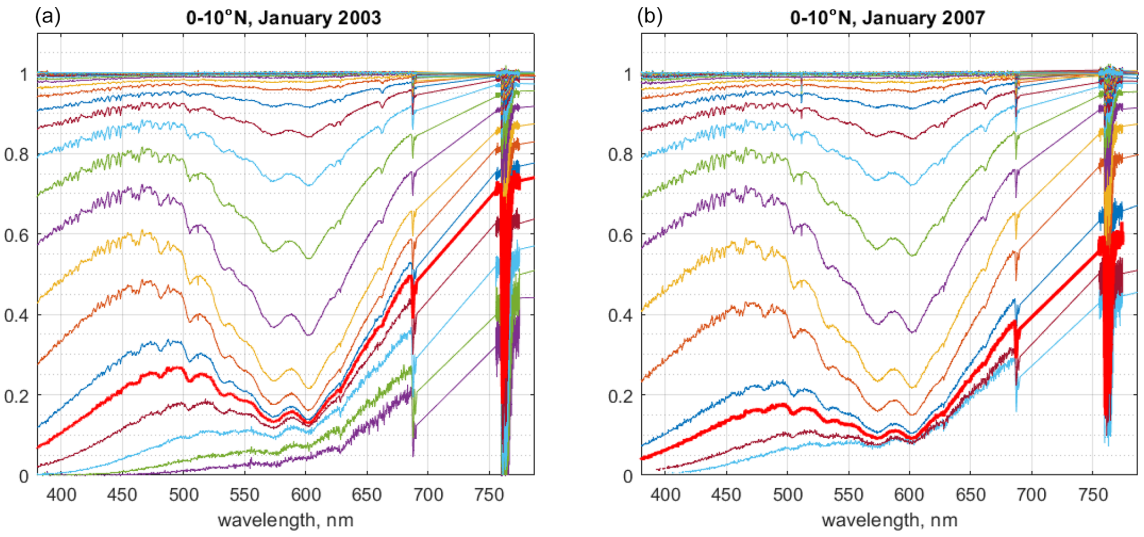

Figure 1. Examples of GOMOS averaged transmittance spectra in the equatorial region 0–10° N, in January 2003 (background aerosols) and in January 2007 (after volcanic eruptions), from 100 km down to the lowest altitude. Thick red lines highlight transmittances at 20 km. For visibility, the transmittance spectra are plotted with a vertical step of 3 km. The lowest altitude is 8 km in panel **(a)** and 14 km in panel **(b)**.

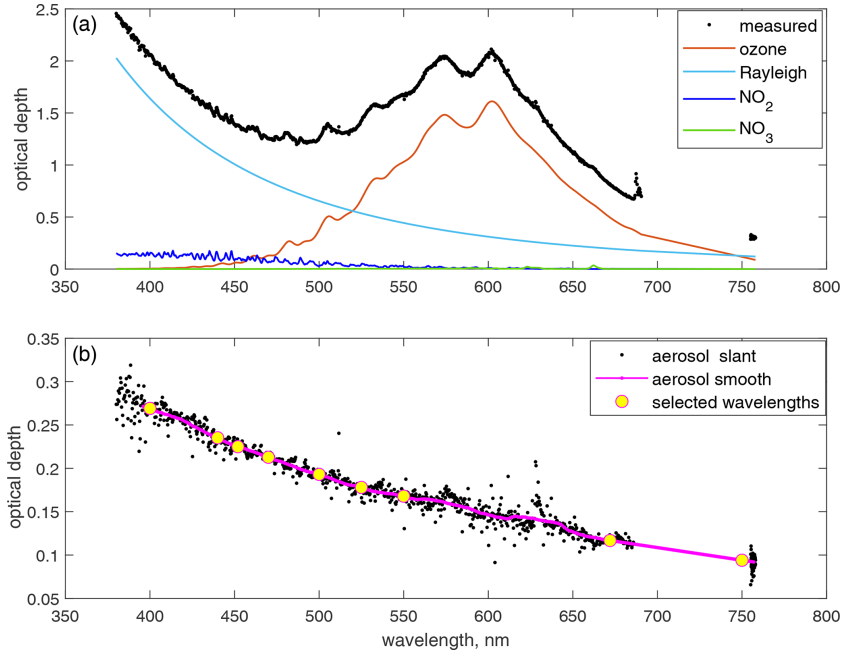

Figure 2. Illustration of the GOMOS aerosol retrieval algorithm. **(a)** Measured optical depth spectrum (black) and contributions due to ozone (red), Rayleigh scattering (cyan), NO_2 (blue) and NO_3(green). **(b)** Original (black) and smoothed (magenta) residuals.

ror propagation of transmittance uncertainties. Typical uncertainties of the retrieved aerosol profiles are shown in Fig. 4.

Examples of retrieved horizontal column optical depth and aerosol extinction profiles are shown in Fig. 3. The retrieved aerosol extinction is larger for shorter wavelengths, as would be expected (e.g., Ångström, 1929; Ramachandran and Jayaraman, 2003). The profiles of the Ångström exponent

$$\alpha = -\frac{\log\left(\frac{\beta(\lambda)}{\beta(\lambda_0)}\right)}{\log\left(\frac{\lambda}{\lambda_0}\right)} \tag{3}$$

for different wavelength combinations are shown in Fig. 3c. The uncertainties of the Ångström exponent are evaluated from uncertainties of retrieved aerosol profiles via error prop-

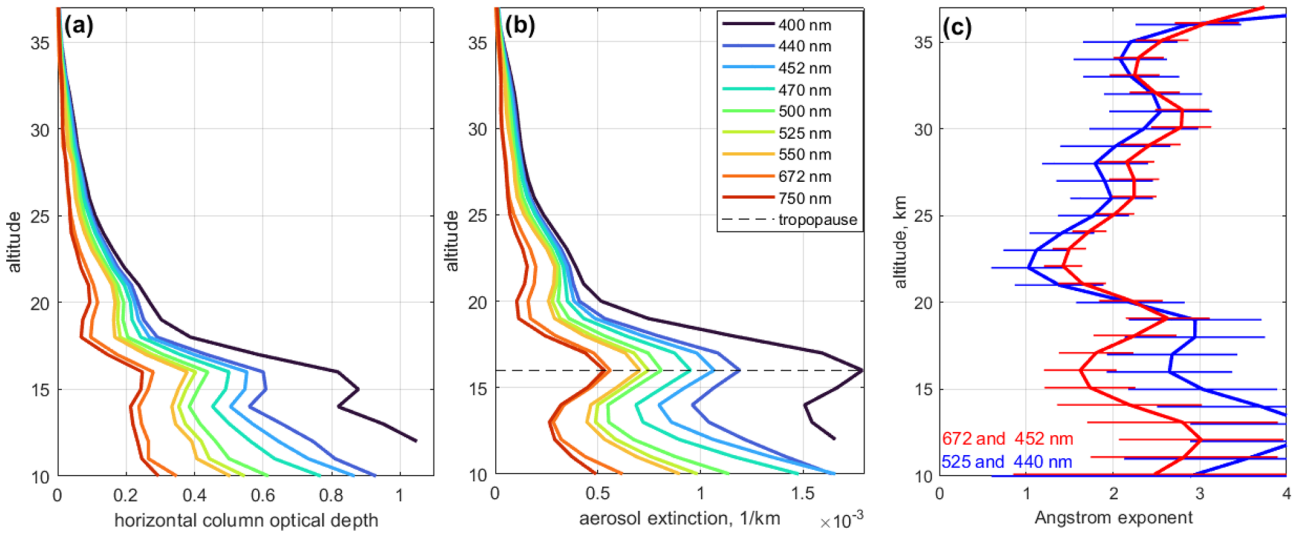

Figure 3. The retrieved horizontal column optical depth **(a)** and aerosol extinction **(b)** for September 2002, 10–20° S (wavelengths are indicated in the legend). **(c)** The Ångström exponent profiles estimated using different combinations of wavelengths. The mean tropopause height is indicated by the dashed black line in panel **(b)**.

agation. The values of the Ångström exponent are in the expected range from 0–0.5 (large particles) to 4 (Rayleigh scattering limit). Above ∼ 22 km, α grows with altitude, becoming closer to the Rayleigh scattering limit, as expected. Below 20 km, the Ångström exponent estimates have large uncertainties, especially when using short wavelengths (e.g., 525 and 440 nm in Fig. 3c). The Ångström exponents estimated using 672 and 452 nm are in the range 1.5–3 below 20 km. The spectral dependence of the retrieved FMI-GOMOSaero aerosol extinction profiles is evaluated and discussed in more detail below.

3 Retrieval results and intercomparisons

The multi-wavelength FMI-GOMOSaero aerosol retrievals can be directly compared with data from other instruments.

In addition to other GOMOS datasets (IPF v6 and AERGOM), we compare our retrievals with aerosol data from SAGE II (Stratospheric Aerosol and Gas Experiment II) on the Earth Radiation Budget Satellite (ERBS), OSIRIS (Optical Spectrograph and InfraRed Imaging System) on Odin and SCIAMACHY (SCanning Imaging Absorption spectroMeter for Atmospheric CHartographY) on Environmental Satellite (Envisat). The aerosol datasets used for intercomparisons are described in Table 1.

For the comparisons, the individual aerosol profiles from SAGE II, OSIRIS, SCIAMACHY and AERGOM are averaged to create monthly zonal mean data. The uncertainties of the monthly mean data are estimated as the standard error of the mean.

The comparisons are focused on a potential use of the new dataset in the merged CREST dataset (Sofieva et al., 2023). Therefore, a special attention is paid to the assessments of validity range, quality of data at 750 nm (they are from the IR spectrometer data, which are usually noisier and affected more by a combined effect of pixel response non-uniformity), and ability to reproduce geophysical variability of stratospheric aerosols.

SAGE II aerosol data are used as a reference in several studies (e.g., Rieger et al., 2015; Kovilakam et al., 2020), and SAGE II provides aerosol extinction profiles at several wavelengths. Therefore, the first example of intercomparison is with SAGE II for the latitude zone 10–20° S in September 2002. Figure 4a–c show FMI-GOMOSaero, SAGE II and AERGOM aerosol extinction profiles at several wavelengths. FMI-GOMOSaero and SAGE II aerosol extinction profiles at 525 nm agree within ±30 % above 20 km (see also Fig. S1 in the Supplement). Below 20 km, GOMOS aerosol extinction is larger, but it is similar to SAGE II extinction with omitted cloud filtering (dashed lines in Fig. 4b and e). AERGOM aerosol extinction profiles also have enhancements near the tropical tropopause, while in the troposphere the AERGOM aerosol extinction coefficients become smaller at shorter wavelengths.

When using averaged transmittances, cirrus cloud cases cannot be excluded, which might result in overestimation of the aerosol extinction below 20 km (see also the discussion below).

Figure 4d–f show aerosol extinction spectra at several altitudes. For SAGE II, both extinctions with (solid lines) and without (dashed lines) cloud filtering are shown. For visual aid, we added values at 750 nm for SAGE II, which are computed using the Ångström-exponent transformation of 525 and 1020 nm data, which are indicated by stars. (Note that

Table 1. Aerosol datasets used for intercomparisons.

Instrument	Measurements/data	Retrieved aerosol parameter(s)	References
SAGE-II v.7 1984–2005	Solar occultation, transmittances in UV–VIS–IR	Aerosol extinction at 386, 452, 525 and 1020 nm	Thomason et al. (2008)
GOMOS AERGOM v.4 2002–2011	Stellar occultation, transmittances in UV–VIS–NIR	Aerosol extinction at 355, 440, 470, 550 and 750 nm; aerosol size distribution	Vanhellemont et al. (2016); Bingen et al. (2017)
OSIRIS v.7 (2001–present)	Limb scattering, radiances in UV–VIS	Aerosol extinctions at 750 nm, the mode radius	Rieger et al. (2014)
SCIAMACHY UBR v.3.0 (2002–2012)	Limb scattering, Sun-normalized radiance at 750 nm, effective surface albedo from collocated nadir measurements	Aerosol extinction at 750 nm	The precursor retrieval version V1.4 is published in Rieger et al. (2018). The differences with V1.4 are described in Sofieva et al. (2023).
SCIAMACHY UBR PSD v2.0 retrievals (2002–2012)	Limb scattering, Sun-normalized radiances in UV–VIS–IR, effective surface albedo from collocated nadir measurements	Particle size distribution	Pohl et al. (2023)

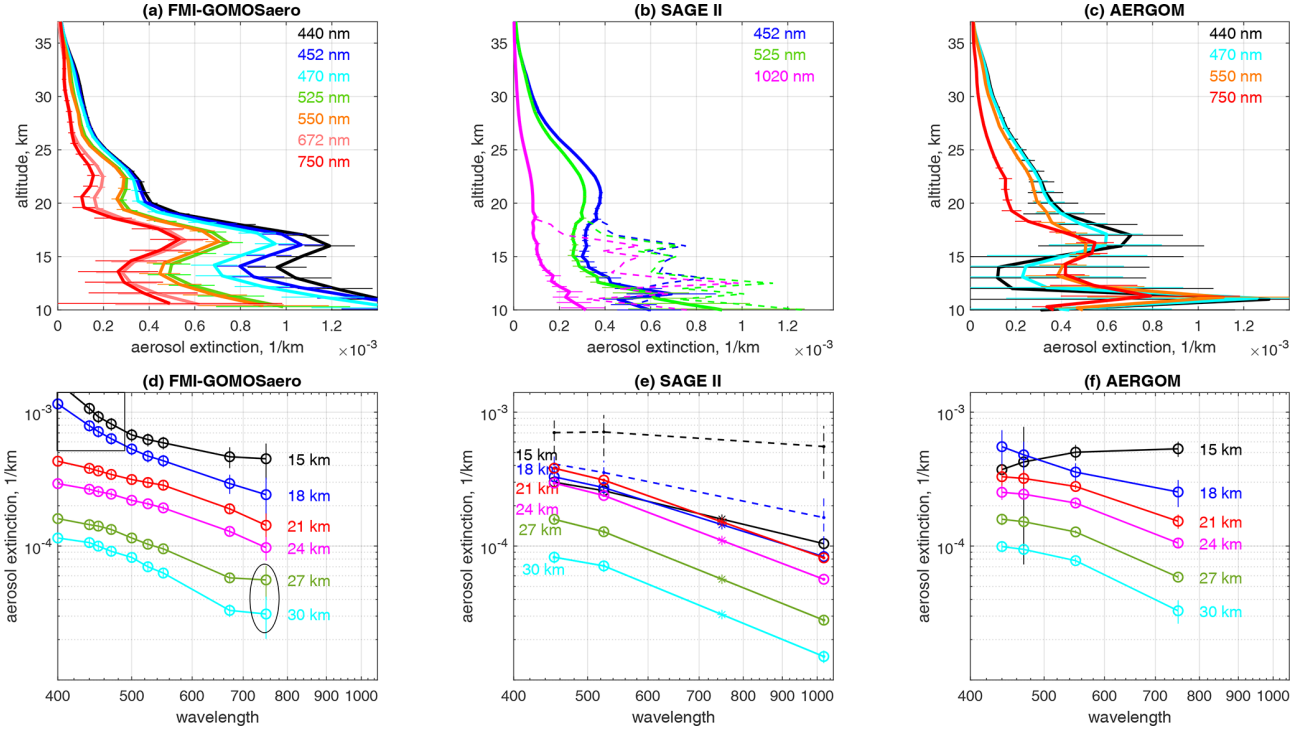

Figure 4. (a–c) Monthly mean aerosol profiles at several wavelengths, September 2002, 10–20° S for FMI-GOMOSaero **(a)**, SAGE II **(b)** and AERGOM v4 **(c)**. The wavelengths are specified in the legend. For SAGE II, profiles with (solid lines) and without cloud filtering (dashed lines) are shown. **(d–f)** Aerosol extinction spectra at selected altitudes specified in the panels. For visual aid, colored stars in panel **(e)** indicate 750 nm aerosol extinction computed using SAGE II extinctions at 525 and 1020 nm. The oval and rectangle in panel **(d)** indicate problematic regions, which are discussed in the main text.

due to the curvature of aerosol extinction spectra, such conversion may introduce a bias, so these 750 nm data should not be considered measurements.) We observe that the shape of aerosol extinction spectra in the lower stratosphere (21 and 24 km) is similar for all three considered datasets.

At upper altitudes, FMI-GOMOSaero spectra have a flattening at 750 nm (black oval in Fig. 4). Although the uncertainty of the 750 nm data is large, it seems to be a systematic feature at upper altitudes. Above 30–32 km, the aerosol extinction at 750 nm is larger than that at 672 nm, and this holds for all NIR GOMOS channels (see also Fig. S2 in the Supplement). Probably, this is related to compatibility of GOMOS UV–VIS and NIR spectrometers. AERGOM does not provide aerosol extinction at 672 nm, so this feature is somewhat obscured in its data, but it is revealed in Ångström exponent estimates using the 750 nm channel (see below).

At lower altitudes, GOMOS data are affected by cirrus clouds, as mentioned above. Although FMI-GOMOSaero extinction spectra in the wavelength range of $\sim$ 525–750 nm have smaller slope at 15 and 18 km than at 21 and 24 km (similarly to SAGE II), the short-wavelength region has, vise versa, a larger slope. At 18 km (near the tropopause), the slopes of aerosol extinction spectra are similar in FMI-GOMOSaero and AERGOM. This suggests that another phenomenon can contribute to observed aerosol enhancements – imperfect refractive dilution correction due to inaccurate ECMWF data (note that very old ECMWF forecast data have been used in the GOMOS processor). Although some improvement is observed when ERA-5 data are used, it does not completely remove the enhancements in the retrieved aerosol extinction near the tropical tropopause. In addition, the GOMOS dilution is estimated using a first-order approximation (Dalaudier et al., 2001), which might not be accurate in the vicinity of the tropical tropopause. This might also be related to an imperfect estimate of Rayleigh scattering. In the troposphere (15 km), AERGOM reports a different shape of the aerosol extinction, with smaller values at shorter wavelengths. Illustrations similar to Fig. 4 but for other latitude zones and time periods can be found in the Supplement.

Figure 5 shows the global distribution of the average Ångström exponent in years 2003–2004 computed using SAGE II, FMI-GOMOSaero and AERGOM data. The mean tropopause, which was evaluated using ERA-5 reanalysis data, is also shown in Fig. 5. Due to the curvature of aerosol extinction spectra, the Ångström exponent depends on wavelengths used for its computation. Therefore, one cannot expect numerical agreement between Ångström exponents evaluated using SAGE 525 and 1020 nm with those obtained from GOMOS data (it is expected to be smaller for the 750 and 525 nm combination in case of background aerosols). Thus, Fig. 5 serves only for comparison of the morphology of Ångström exponent. For SAGE II, Ångström exponent increases with altitude in the stratosphere, with typical values of $\sim$ 2 in the middle stratosphere. For FMI-GOMOSaero, a similar behavior is observed for both combinations 672 and 470 nm and 672 and 470 nm until altitudes of $\sim$ 30–32 km. Above 30–32 km, we observe a decrease of Ångström exponent in the tropics and at mid-latitudes, which is strong when data at 750 nm are used. At these altitudes, data have very large uncertainty; thus, Ångström exponent estimates also have large uncertainty (crosses mark estimates with uncertainty exceeding 100 %), so they should be considered unreliable in this altitude range. For AERGOM, a similar drop of Ångström exponent is observed at altitudes above 30–32 km. This is consistent with analyses of aerosol extinction spectra discussed above and indicates its instrumental origin. In the tropical troposphere, a reduction of Ångström exponent is observed, but FMI-GOMOSaero values are larger, while AERGOM values are smaller than those of SAGE II. This region is affected by cirrus clouds, which are difficult to separate from aerosols due to a limited wavelength range of GOMOS measurements, and uncertainties of GOMOS estimates are large in this region for both GOMOS datasets. The AERGOM distribution of Ångström exponent exhibits an enhanced layer above the tropopause, which is not observed in SAGE II or FMI-GOMOSaero distributions.

In the following illustrations, we will concentrate on comparison of aerosol profiles in the stratosphere.

Examples of FMI-GOMOSaero profiles are shown in Fig. 6 together with the averaged profiles from several other satellite instruments for several latitude zones and time periods. At 525 nm, our retrievals are compared with AERGOM (at 550 nm), SAGE II and SCIAMACHY measurements. At 750 nm, FMI-GOMOSaero aerosol profiles are compared with AERGOM, SCIAMACHY and OSIRIS data. In both comparisons, the SCIAMACHY data from the special retrievals with the reconstruction of the particle size distribution (Malinina et al., 2018; Pohl et al., 2023) are shown with cyan lines. The blue line in the bottom panels of Fig. 7 corresponds to nominal SCIAMACHY UBR v3.0 retrievals. In the bottom panels of Fig. 6, SAGE II profiles, which are converted to 750 nm from 525 and 1020 nm using Ångström exponent with a correction described in Damadeo et al. (2023) and Sofieva et al. (2023), are shown by dashed black lines.

Figure 7 shows a comparison of the monthly zonal mean FMI-GOMOSaero aerosol extinction coefficients globally at 21.5 km with analogous values from SAGE II, OSIRIS and SCIAMACHY. In Fig. 7b, SAGE II data are converted to 750 nm using its 525 and 1020 nm data, as explained above. For 750 nm (Fig. 7b, c, e, and f), we used two collections of FMI-GOMOSaero data: retrieved at 750 nm (red) and converted from 672 nm via the Ångström exponent, which is evaluated using 672 and 500 nm (blue). In the panels, the number of collocated monthly zonal mean data N, correlation coefficient R, the overall mean of relative differences $\mathrm{RD} = \frac{\text{FMI-GOMOSaero}-\text{instrument}}{\text{FMI-GOMOSaero}+\text{instrument}} \cdot 200\,\%$ (bias) and their standard deviation (spread) are specified. Dashed lines are linear regression lines. As observed in Fig. 7, FMI-GOMOSaero data converted from 672 nm have better correlations with the other datasets and smaller spreads with respect to them,

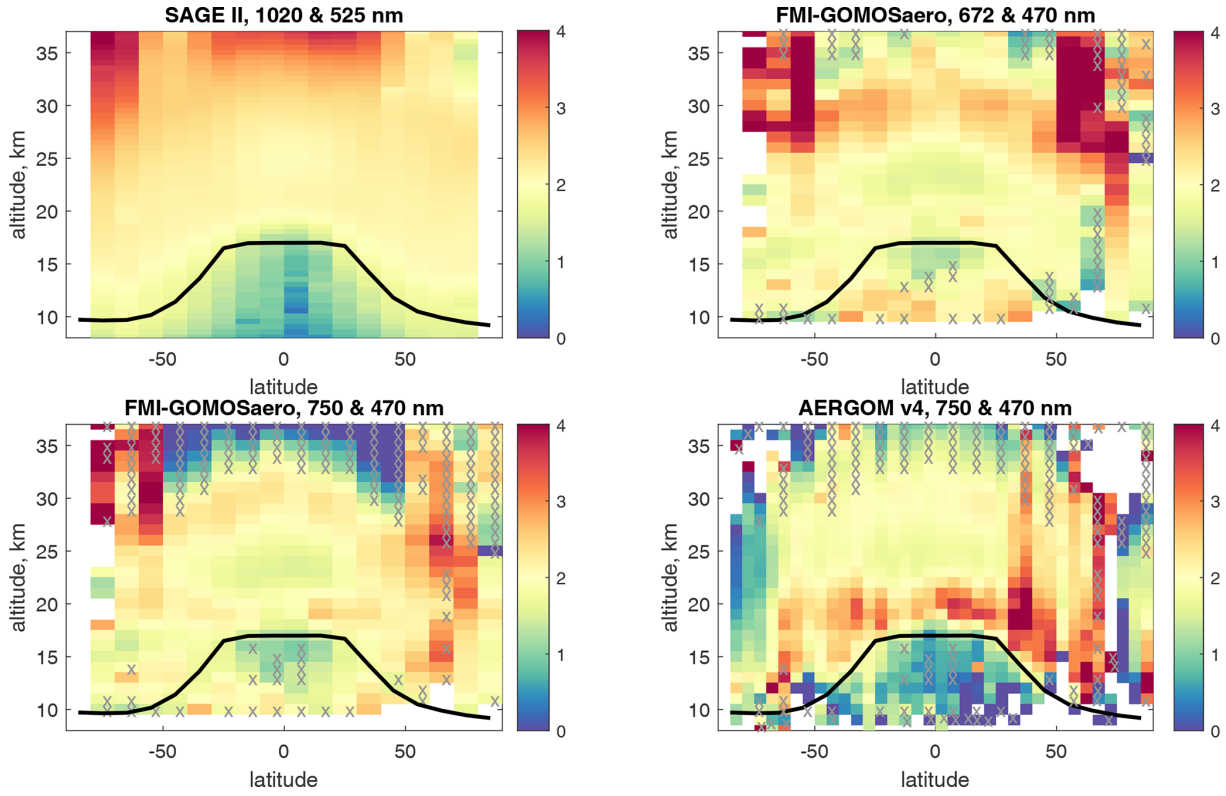

Figure 5. Average Ångström exponent in 2003–2004 computed using SAGE II, FMI-GOMOSaero and AERGOM data. Wavelength combinations and instruments are indicated in the panels. The data with average estimated uncertainty exceeding 100 % are marked with gray crosses. Black lines indicate mean tropopause. Empty boxes for AERGOM correspond to negative aerosol extinction data for which the Ångström exponent has not been evaluated. SAGE II data are cloud filtered.

compared to data retrieved at 750 nm. In comparison with OSIRIS and SCIAMACHY, where both background and enhanced aerosol conditions are observed, the correlation coefficients are 0.83 with respect to OSIRIS and 0.76 with respect to SCIAMACHY. In comparison with SAGE II, the aerosol extinctions are smaller in the overlapping 3 years, and the correlation coefficient between SAGE II and FMI-GOMOSaero data at 525 nm is 0.72. The overall biases at 21.5 km are less than 1 % with respect to SAGE II at 525 nm, and a few percent with respect to OSIRIS and SCIAMACHY. The spread is ∼ 20 %–30 %.

The statistical behavior of relative differences (RD) between FMI-GOMOSaero and other datasets are shown for 525 nm in Fig. 8 and for 750 nm in Fig. 9. The differences are computed for all monthly zonal mean values available in the datasets. The colored lines in Figs. 8 and 9 show the median, and horizontal bars indicate the range between 16th and 84th percentiles of the distribution. The comparisons are shown for three latitude regions: tropics 20° S–20° N (Figs. 8b and 9b, e, h), southern mid-latitudes 30–60° S (Figs. 8a and 9a, d, g) and northern mid-latitudes 30–60° N (Figs. 8c and 9c, f, i). In Fig. 8, comparisons with SAGE II and SCIAMACHY PSD are for 525 nm. In comparison with AERGOM, both FMI-GOMOSaero and AERGOM data at 550 nm are used. The gray shading shows the region of tropical troposphere, which is affected by clouds as discussed earlier. With respect to SAGE II and AERGOM, the biases shown in Fig. 8 progress from positive values in the lowermost stratosphere to negative values above 27 km for all latitude zones. With respect to SAGE II, FMI-GOMOSaero biases are within ±10 % at 20–25 km and increase to ±20 %–40 % at upper and lower altitudes. The biases with respect to SCIAMACHY are similar to SAGE II but negative at altitudes 18–35 km.

Figure 9 shows the analogous statistics of relative differences but for 750 nm. We used three GOMOS aerosol datasets: FMI-GOMOSaero data retrieved at 750 nm (Fig. 9a–c), FMI-GOMOSaero converted from 672 to 750 nm (Fig. 9d–f) and AERGOM v4 at 750 nm (Fig. 9g–i). SAGE II data used in the comparison are converted to 750 nm from 525 and 1020 nm using Ångström exponent with a correction described in Damadeo et al. (2023) and Sofieva et al. (2023). For 750 nm, FMI-GOMOSaero biases with respect to other datasets are mainly within 20 %–40 % (excluding the tropical troposphere region). The best agreement and similar structure of biases are observed with respect to OSIRIS, converted SAGE II and SCIAMACHY PSD. Comparing the top and central panels of Fig. 9, one

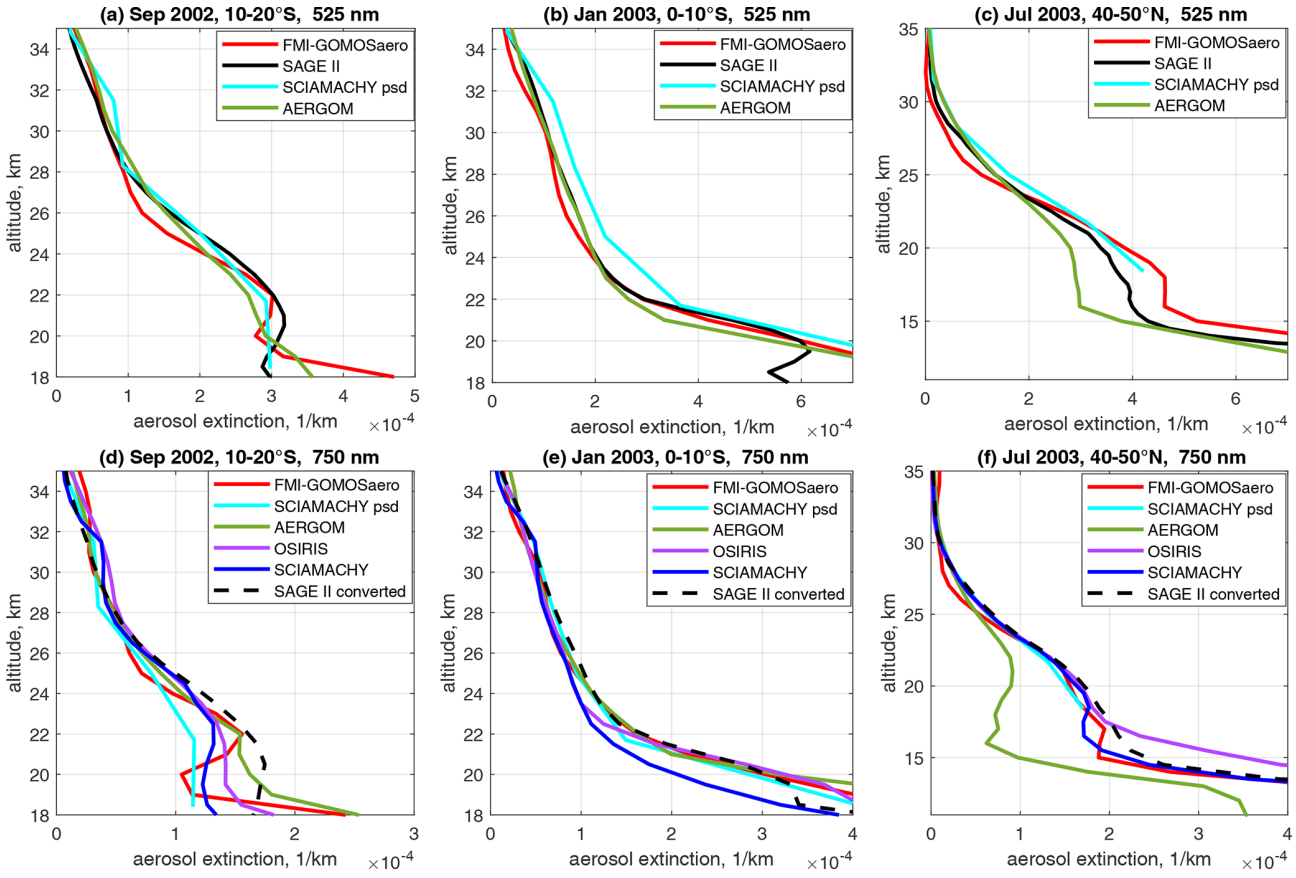

Figure 6. Comparison of new GOMOS retrieved profiles with data from several satellite instruments. **(a–c)** Comparisons for the wavelength 525 nm; **(d–f)** comparisons for the wavelength 750 nm. The datasets are specified in the legend. The dates and latitudes are indicated in the panel titles.

can notice smaller biases and inter-percentile range for FMI-GOMOSaero data converted to 750 nm from 672 nm.

A similar analysis of relative differences but for AERGOM v4 data is shown in the bottom panels of Fig. 9. The overall structure of AERGOM biases with respect to other datasets differs from that of FMI-GOMOSaero: they are similar in the tropics but larger at mid-latitudes. The inter-percentile range of the AERGOM relative differences to other datasets is larger, especially at mid-latitudes, which indicates improvements in the proposed dataset.

4 FMI-GOMOSaero aerosol climate data record

The entire GOMOS dataset has been processed. Subsequently, we filtered out the data points that have unrealistic values for the Ångström exponent ($\alpha > 4$ below 27 km) or are potentially affected by clouds ($\alpha < -0.2$). This mild filtering is aimed at removal of strong outliers. Other data are characterized by uncertainty estimates.

By examining outliers in the processed GOMOS-FMI aerosol dataset, we found that one of the reasons for strong outliers is an insufficient amount of data available for transmittance averaging. Therefore, the data based on a small number of averaged transmittances (less than 20) are excluded from the final GOMOS aerosol dataset.

Figure 10 shows the time series of stratospheric aerosol extinction for 672 nm at three altitude levels in the stratosphere. The main aerosol events (volcanic eruptions and wildfires) during 2002–2012 (see Table 2) are indicated in Fig. 10 by black circles of the size proportional to their volcanic explosivity index (VEI). Volcanic eruption signatures are clearly seen in 2007, 2009 and 2010. The enhancements are more pronounced at 17 km, as expected. The largest enhancement at 21 km is in the tropics, and it is associated with Soufrière Hills and Rabaul/Tavurvur volcanic eruptions in 2006. At 25 km, the aerosols have significantly smaller variations; one can notice gradually increasing aerosol extinction at this altitude during the GOMOS operating period.

Figure 10 also illustrates the coverage by GOMOS data. There is less data at lower altitudes; this is associated with the lowest probed altitude, which depends on stellar brightness. One can also notice a decrease of data coverage after 2009, which is related to a decreased number of GOMOS

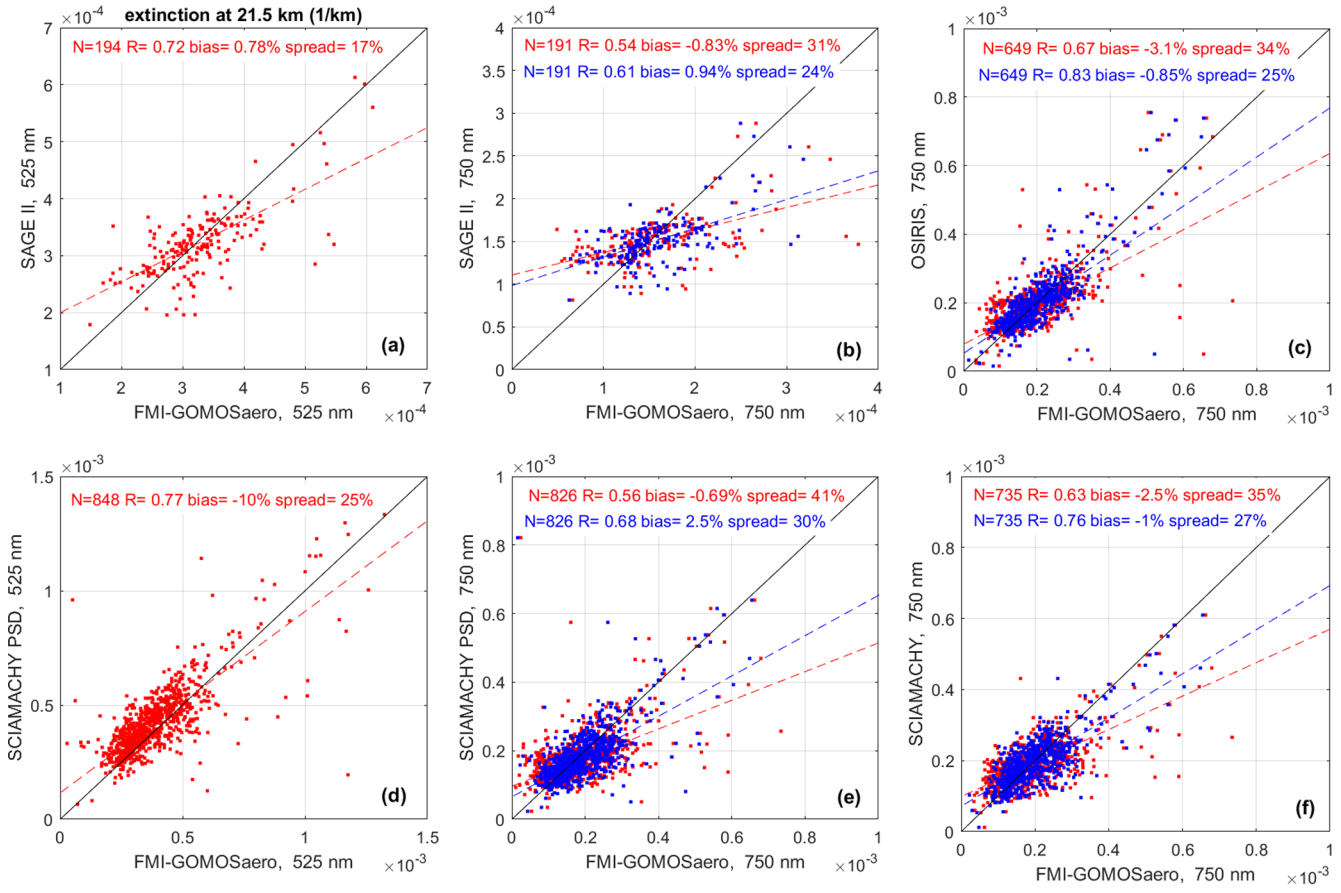

Figure 7. Comparison of monthly zonal mean FMI-GOMOSaero aerosol extinction coefficients at 21.5 km with analogous values from **(a)** SAGE II at 525 nm, **(b)** OSIRIS at 750 nm, **(c)** SAGE II converted to 750 nm using its 525 and 1020 nm data (see the main text for explanation), and **(d)** SCIAMACHY v3.0. In panels **(b)**–**(d)**, the retrieved 750 nm FMI-GOMOSaero data are shown in red, while the data converted from 672 nm are shown in blue.

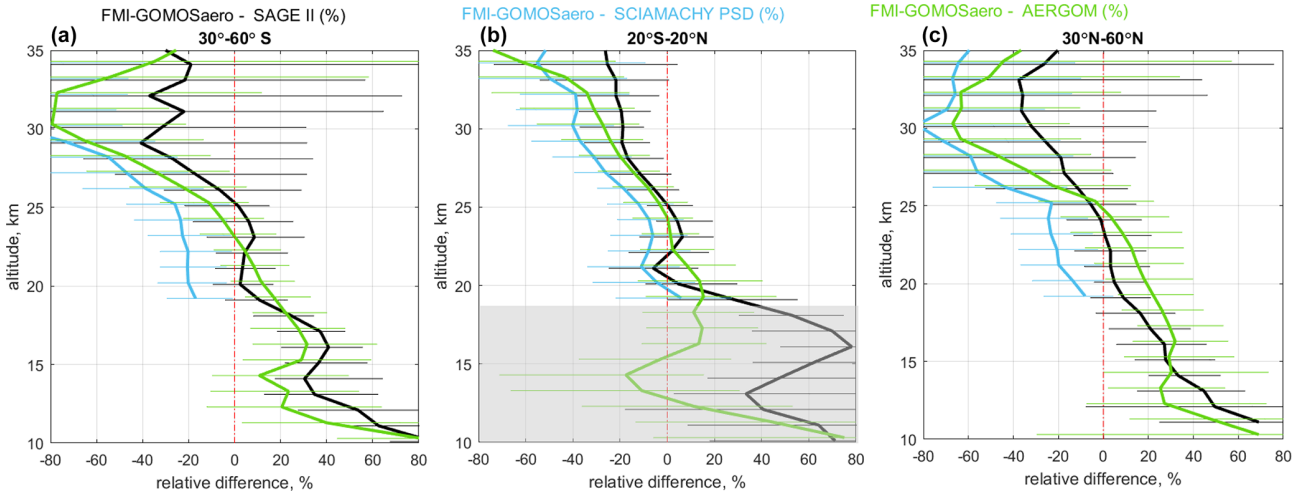

Figure 8. Median (solid lines) and 16th and 84th percentiles (horizontal bars) of relative differences between FMI-GOMOSaero and other datasets for latitudes 30–60° S **(a)**, 20° S–20° N **(b)** and 30–60° N **(c)**. Comparison with SAGE II and SCIAMACHY PSD are for 525 nm. In comparison with AERGOM, data at 550 nm are used. The gray shading shows the region of the tropical troposphere.

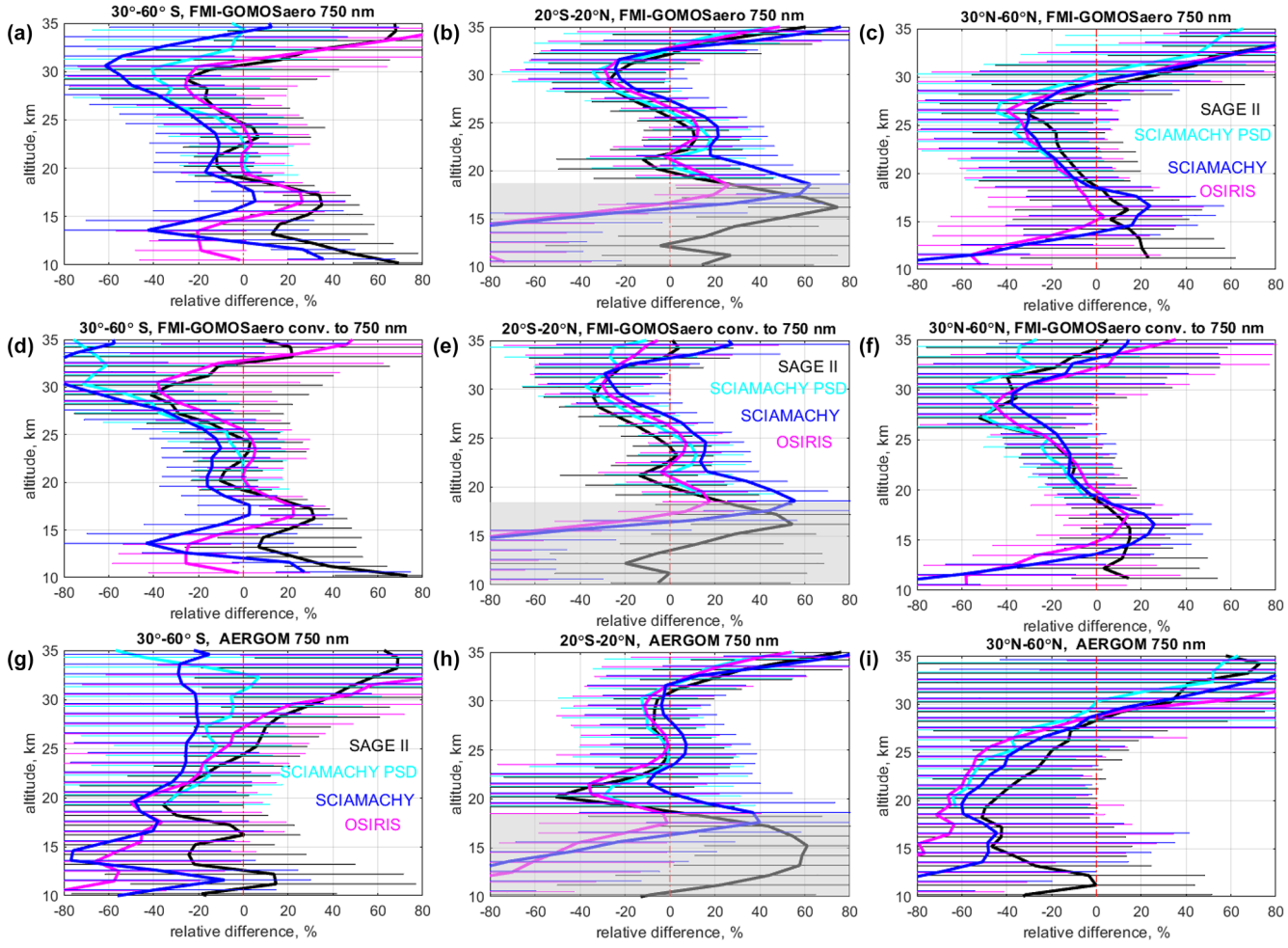

Figure 9. Same as Fig. 8 but comparisons are for 750 nm and for three GOMOS datasets: FMI-GOMOSaero data retrieved at 750 nm **(a–c)**, FMI-GOMOSaero converted from 672 to 750 nm **(d–f)** and AERGOM v4 at 750 nm **(g–i)**. SAGE II data are converted to 750 nm (see the main text for the explanation).

Table 2. The list of volcanic eruptions and strong wildfires.

Year	Month	Volcano/wildfire name	Abbreviation	Latitude (°)	VEI	Max plume altitude (km)
2002	11	Reventador	Re	0	4	17
2004	11	Manam	Ma	4	4	18–24
2006	5	Soufrière Hills	So	16	4	17
2006	10	Rabaul/Tavurvur	Ta	−4	4	18
2008	5	Chaitén	Cha	−42	4	16.8
2008	7	Okmok	Ok	55	4	15
2008	8	Kasatochi	Ka	55	4	14
2009	2	Fire/Victoria	Vi	−37	3	
2009	6	Sarychev	Sa	48	4	21
2010	11	Merapi	Me	−8	4	18.3
2011	5	Grimsvótn	Gr	64	4	20
2011	6	Nabro	Na	13	4	13.7
2011	7	Cordon Caulle	CC	−40	5	14

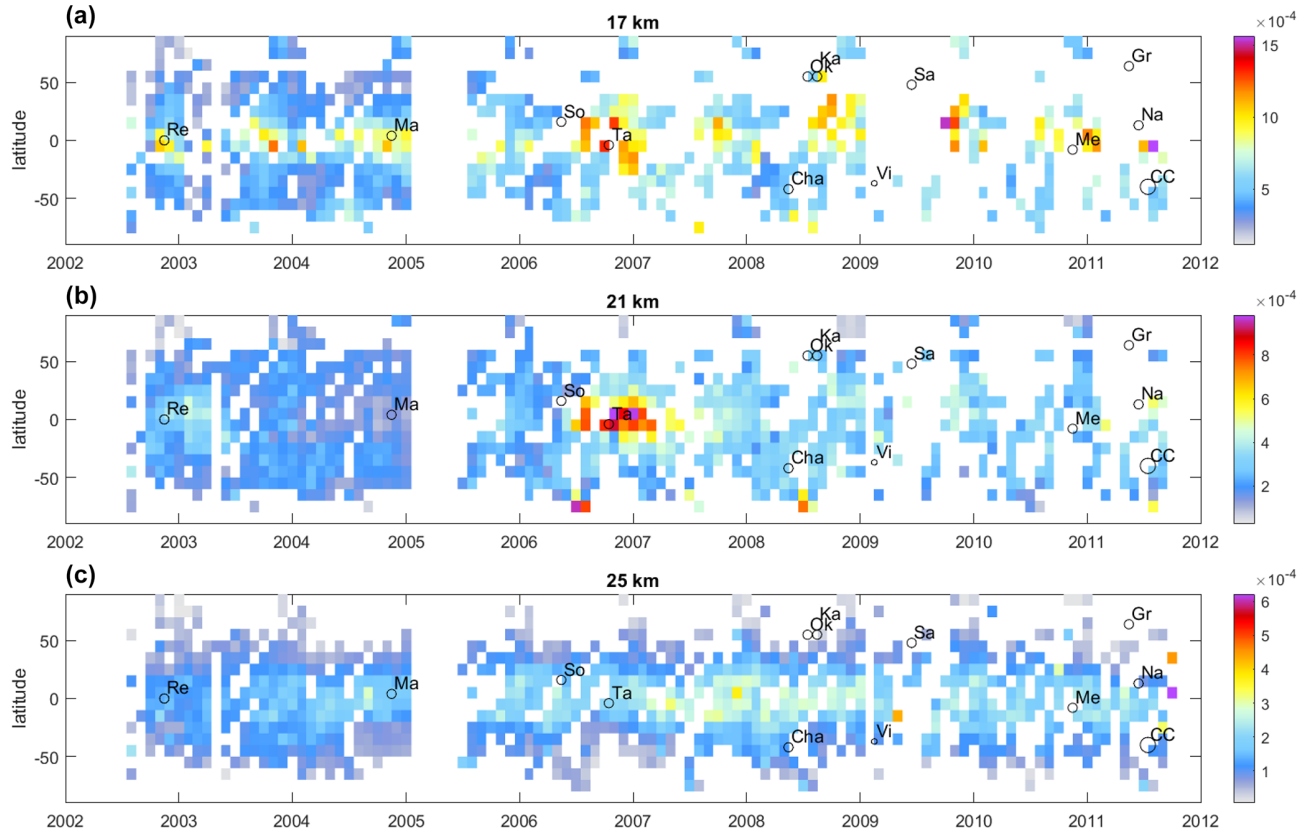

Figure 10. Time series of aerosol extinction ($1\,km^{-1}$) at 672 nm for 17 km **(a)**, 20 km **(b)** and 25 km **(c)**. Main aerosol events (volcanic eruptions and wildfires) are indicated by black circles of the size proportional to their volcanic explosivity index (VEI).

measurements due to instrumental problems (Bertaux et al., 2010).

Figure 11 shows the time series of aerosol extinction at 20 km in the latitude zones 30–60° S (Fig. 11a), 20° S–20° N (Fig. 11b) and 30–60° N (Fig. 11c) for all retrieved wavelengths. Aerosol extinction coefficient decreases with wavelength. The enhancements due to volcanic eruptions – Reventador in 2002, Soufrière Hills and Rabaul/Tavurvur in 2006 and Okmok and Kasatochi in 2008 – are seen in the data.

Figure 12 shows an analogous time series of aerosol extinction as shown in Fig. 11 but using AERGOM v4 data. The AERGOM data are filtered in the same way as FMI-GOMOSaero and shown for the same latitude–time bins that are present in the FMI-GOMOSaero dataset. The time series of AERGOM data without additional filtering (i.e., based on data which are reported as valid in the AERGOM files) is shown in the Supplement (Fig. S5). After 2009, AERGOM aerosol extinction sometimes does not decrease with wavelength. Furthermore, AERGOM often reports negative aerosol extinction at 440 and 750 nm, especially after 2009 (however, the retrieval uncertainties characterize well the AERGOM data, as discussed earlier). The enhancements related to volcanic eruptions are visible in AERGOM, but they are less pronounced compared to the FMI-GOMOSaero dataset.

In order to use GOMOS aerosol profile time series in the merged Climate Data of Stratospheric Aerosols (CREST; Sofieva et al., 2023), the data at 750 nm are needed. FMI-GOMOSaero retrievals provide aerosol profiles at 750 nm. However, our intercomparison studies have shown that the FMI-GOMOSaero data converted to 750 nm from 672 nm have smaller biases and spread and higher correlation with other datasets, compared to retrieved aerosol extinction coefficients at 750 nm. In general, this is not surprising, as GOMOS IR spectrometer data are noisier, and they are affected by detector non-uniformity. As an additional illustration of various GOMOS datasets, we show in Fig. 13 the 750 nm GOMOS aerosol extinction time series computed by different methods: either retrieved at 750 nm or computed from other wavelengths. The latter method was applied using Eq. (3) with the value of Ångström exponent set to 2.29, a value representative for typical stratospheric aerosol particle size distributions according to Malinina et al. (2019). These time series, which are computed using FMI-GOMOSaero aerosols, IPF v6 and AERGOM, are presented in Fig. 13, together with the merged aerosol dataset, which is computed as the median of SAGE II, OSIRIS and SCIAMACHY data (an

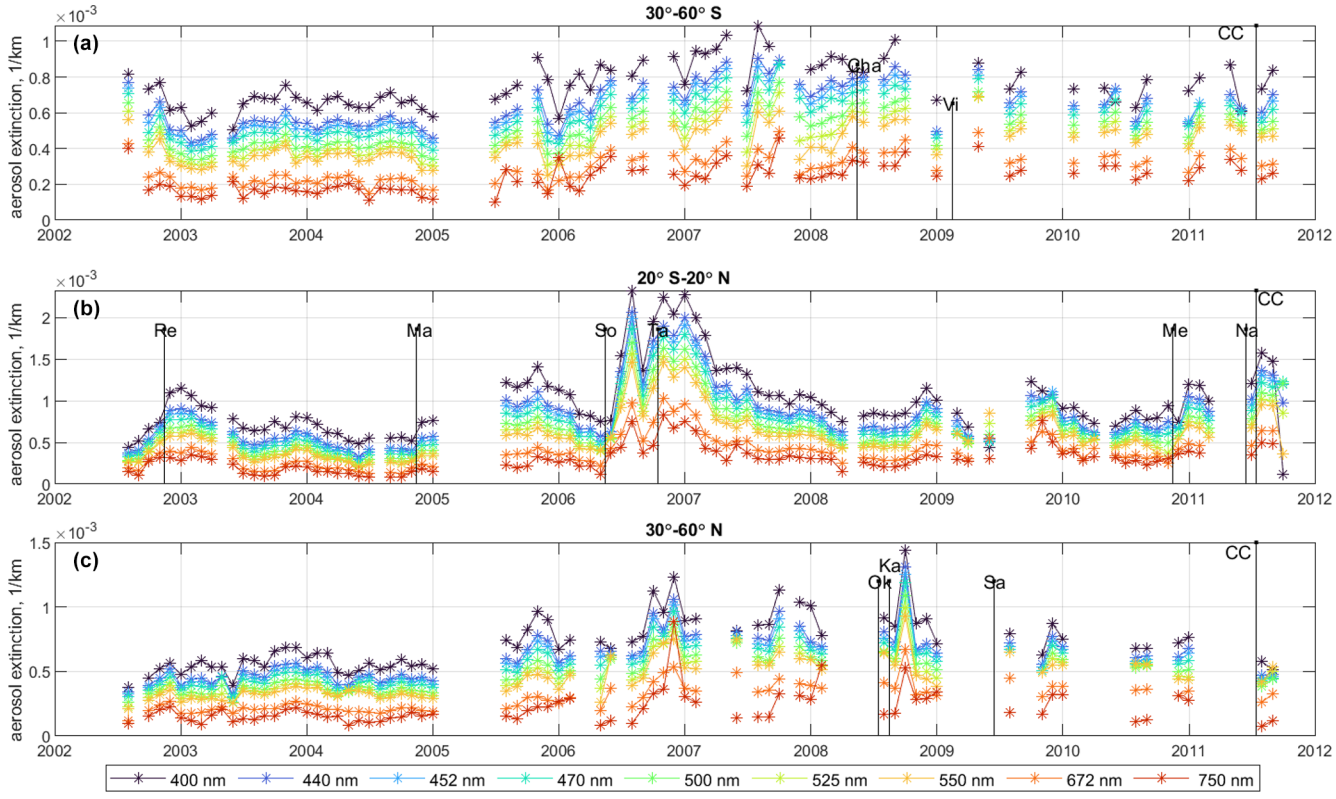

Figure 11. Time series of FMI-GOMOSaero aerosol extinction ($1\,km^{-1}$) at 20 km in the latitude zones 30–60° S **(a)**, 20° S–20° N **(b)** and 30–60° N **(c)**. The wavelengths are indicated in the figure legend. The volcanos are indicated by black bars with the length proportional to volcanic explosivity index (VEI). Volcanos with VEI ≥ 5 are shown for all latitude zones and with VEI > 3 in the corresponding latitude zones.

illustration of individual datasets before data merging can be found in Sofieva et al., 2023). In Fig. 13, AERGOM data are shown only for the same times that they are present in FMI-GOMOSaero. A similar time series but with all AERGOM data reported as valid is shown in the Supplement (Fig. S6). In this illustration, FMI-GOMOSaero aerosol extinction data measured at 750 nm and converted from 672 nm are rather close to each other compared to the merged dataset (and they are closer to the merged dataset than other variants of data and their conversion). However, based on statistical analyses presented in the paper, we recommend FMI-GOMOSaero data transformed to 750 nm from 672 nm with the aid of the retrieved Ångström exponent for using in the merged CREST aerosol climate data record.

5 Summary

An aerosol retrieval algorithm from averaged transmittance spectra has been developed and applied to the GOMOS nighttime dataset. It uses the standard GOMOS two-step retrieval strategy: the spectral inversion is followed by the vertical inversion. The spectral inversion relies on the removal of contributions from ozone, NO_2, NO_3 and Rayleigh scattering from the optical depth spectra for each ray perigee altitude. The remaining slant optical depth is due to stratospheric aerosols. In the vertical inversion, the profiles of aerosol extinction coefficients at several individual wavelengths are retrieved from the profiles of aerosol horizontal column optical depths.

The new aerosol extinction profiles (FMI-GOMOSaero dataset v.1) are provided in the altitude range 10–40 km at wavelengths of 400, 440, 452, 470, 500, 525, 550, 672 and 750 nm. The data are monthly averaged in 10° latitude bands from 90° S to 90° N for the whole GOMOS operating period from August 2002 to March 2012. Intercomparisons of the retrieved FMI-GOMOSaero aerosol profiles with aerosol profile data from other satellite instruments found the average difference within 20 %–40 % in the lower and middle stratosphere, the standard deviation to be ∼ 20 %–50 %, and the correlation coefficient of time series to be 0.65–0.85. Aerosol enhancements during volcanic eruptions are clearly seen in the FMI-GOMOSaero aerosol time series.

The FMI-GOMOSaero monthly mean aerosol extinction profiles can also be used as a priori information for individual GOMOS retrievals. This can be the subject of future work.

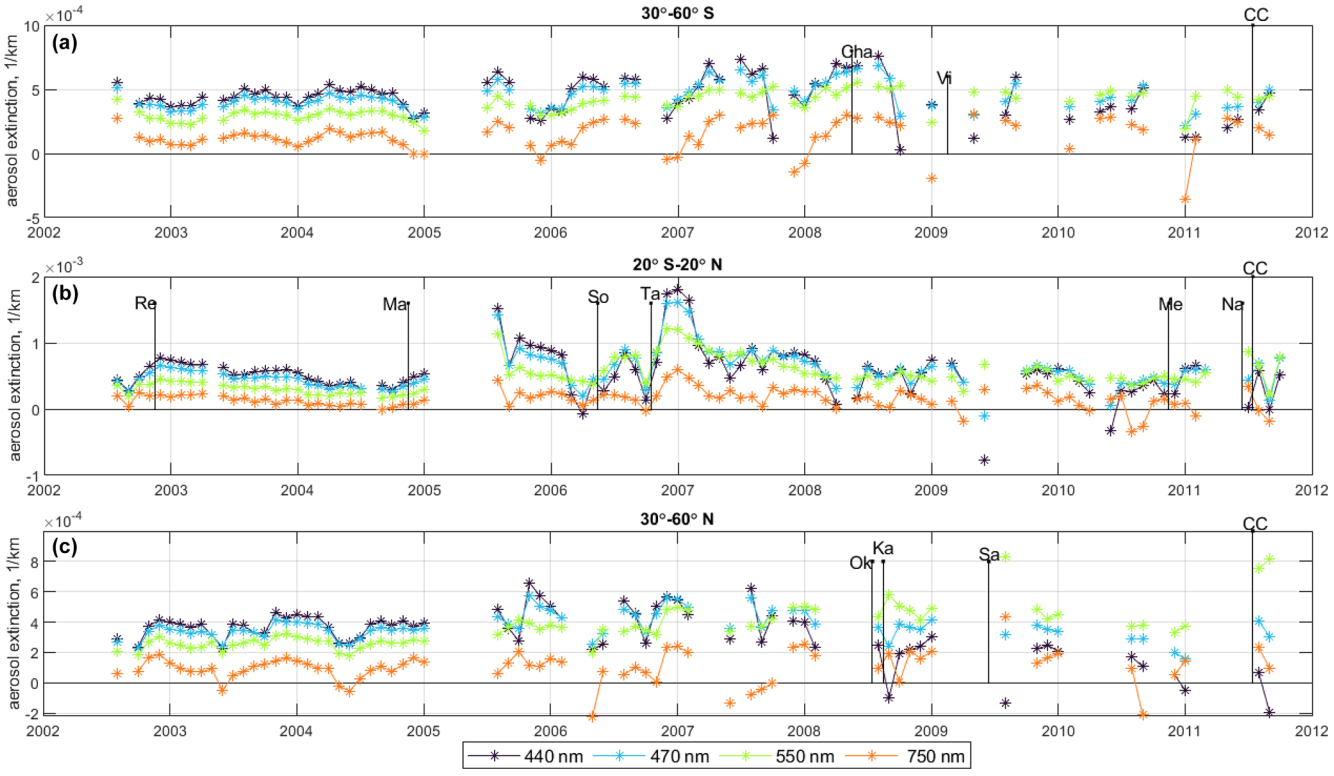

Figure 12. Same as Fig. 11 but for the AERGOM v.4 aerosol extinction. AERGOM data are shown only for the same latitude bins and times that are present in the FMI-GOMOSaero data.

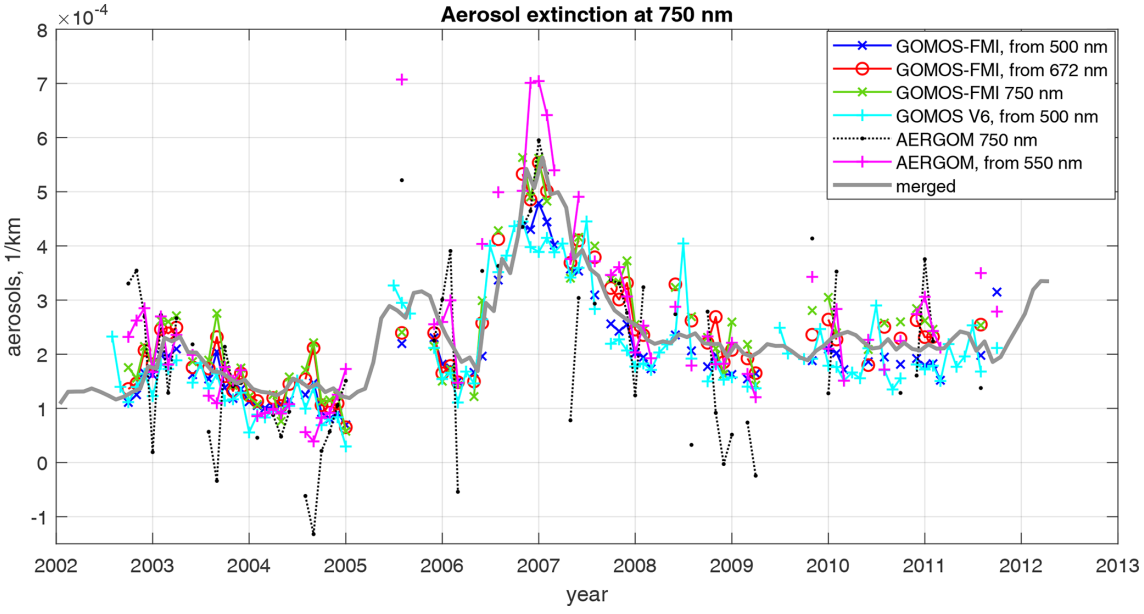

Figure 13. GOMOS aerosol extinction at 750 nm computed by different methods: GOMOS-FMI retrieved at 750 nm (green), GOMOS-FMI converted from 672 nm (red), GOMOS-FMI converted from 500 nm (blue), GOMOS IPF v6 converted from 500 nm (cyan), and AERGOM retrieved at 750 nm (black) and converted from 550 nm (magenta). Thick gray line indicates merged aerosol extinction. All time series are for the latitude bin 0–10° N and altitude of 22 km. AERGOM data are shown only for the same times that are present in the FMI-GOMOSaero data.

Data availability. The FMI-GOMOSaero dataset is available at https://doi.org/10.57707/FMI-B2SHARE.46080A1FCE064E71975EA61C9E839721 (Sofieva, 2023).

Supplement. The supplement related to this article is available online at: https://doi.org/10.5194/amt-17-3085-2024-supplement.

Author contributions. VFS designed the study, performed the analyses, created the dataset and wrote the majority of the paper. DF provided the method and the software for averaging GOMOS transmittances. CB, FV, and NM provided the AERGOM dataset and expertise on its use. AR and CP provided the SCIAMACHY data. MS collected the database of volcanic eruptions. All co-authors contributed to data analyses and writing of the paper.

Competing interests. The contact author has declared that none of the authors has any competing interests.

Disclaimer. Publisher's note: Copernicus Publications remains neutral with regard to jurisdictional claims made in the text, published maps, institutional affiliations, or any other geographical representation in this paper. While Copernicus Publications makes every effort to include appropriate place names, the final responsibility lies with the authors.

Acknowledgements. The work is performed in the framework of ESA project CREST. The creation of the SCIAMACHY aerosol dataset at the University of Bremen was funded in part by ESA via the CREST project, by the German Research Foundation (DFG) via the Research Unit VolImpact (grant no. FOR2820), and by the University of Bremen and state of Bremen. The University of Bremen team gratefully acknowledges the computing time granted by the Resource Allocation Board and provided on the supercomputers Lise and Emmy at NHR@ZIB and NHR@Göttingen as part of the Nationales Hochleistungsrechnen (NHR) infrastructure. The calculations for this research were conducted with computing resources under the project hbk00098. The FMI team thanks the Academy of Finland (Centre of Excellence of Inverse Modelling and Imaging; decision 353082).

Financial support. This research has been supported by the European Space Agency (project CREST, contract no. 4000130839/20/I-DT) and the Research Council of Finland (Centre of Excellence of Inverse Modelling and Imaging; decision 353082).

Review statement. This paper was edited by Andrew Sayer and reviewed by Robert Damadeo and one anonymous referee.

References

Ångström, A.: On the Atmospheric Transmission of Sun Radiation and on Dust in the Air, Geogr. Ann., 11, 156, https://doi.org/10.2307/519399, 1929.

Bertaux, J. L., Kyrölä, E., Fussen, D., Hauchecorne, A., Dalaudier, F., Sofieva, V., Tamminen, J., Vanhellemont, F., Fanton d'Andon, O., Barrot, G., Mangin, A., Blanot, L., Lebrun, J. C., Pérot, K., Fehr, T., Saavedra, L., Leppelmeier, G. W., and Fraisse, R.: Global ozone monitoring by occultation of stars: an overview of GOMOS measurements on ENVISAT, Atmos. Chem. Phys., 10, 12091–12148, https://doi.org/10.5194/acp-10-12091-2010, 2010.

Bingen, C., Robert, C. E., Stebel, K., Brühl, C., Schallock, J., Vanhellemont, F., Mateshvili, N., Höpfner, M., Trickl, T., Barnes, J. E., Jumelet, J., Vernier, J.-P., Popp, T., De Leeuw, G., and Pinnock, S.: Stratospheric aerosol data records for the climate change initiative: Development, validation and application to chemistry-climate modelling, Remote Sens. Environ., 203, 296–321, https://doi.org/10.1016/j.rse.2017.06.002, 2017.

Brühl, C., Schallock, J., Klingmüller, K., Robert, C., Bingen, C., Clarisse, L., Heckel, A., North, P., and Rieger, L.: Stratospheric aerosol radiative forcing simulated by the chemistry climate model EMAC using Aerosol CCI satellite data, Atmos. Chem. Phys., 18, 12845–12857, https://doi.org/10.5194/acp-18-12845-2018, 2018.

Dalaudier, F., Kan, V., and Gurvich, A. S.: Chromatic refraction with global ozone monitoring by occultation of stars. I. Description and scintillation correction, Appl. Optics, 40, 866–877, 2001.

Damadeo, R. P., Sofieva, V. F., Rozanov, A., and Thomason, L. W.: An Empirical Characterization of the Aerosol Ångström Exponent Interpolation Bias using SAGE III/ISS Data, Atmos. Meas. Tech. Discuss. [preprint], https://doi.org/10.5194/amt-2023-260, in review, 2023.

Edgeworth, F. Y.: XXII. On a new method of reducing observations relating to several quantities, London, Edinburgh, and Dublin Philosophical Magazine and Journal of Science, 25, 184–191, https://doi.org/10.1080/14786448808628170, 1888.

Fussen, D., Vanhellemont, F., Dodion, J., Bingen, C., Mateshvili, N., Daerden, F., Fonteyn, D., Errera, Q., Chabrillat, S., Kyrölä, E., Tamminen, J., Sofieva, V. F., Hauchecorne, A., Dalaudier, F., Bertaux, J. L., Renard, J.-B., Fraisse, R., d'Andon, O. F., Barrot, G., Guirlet, M., Mangin, A., Théodore, B., P, Snoeij, and Saavedra, L.: A global OClO stratospheric layer discovered in GOMOS stellar occultation measurements, Geophys. Res. Lett., 33, L13815, https://doi.org/10.1029/2006GL026406, 2006.

Fussen, D., Vanhellemont, F., Tétard, C., Mateshvili, N., Dekemper, E., Loodts, N., Bingen, C., Kyrölä, E., Tamminen, J., Sofieva, V., Hauchecorne, A., Dalaudier, F., Bertaux, J.-L., Barrot, G., Blanot, L., Fanton d'Andon, O., Fehr, T., Saavedra, L., Yuan, T., and She, C.-Y.: A global climatology of the mesospheric sodium layer from GOMOS data during the 2002–2008 period, Atmos. Chem. Phys., 10, 9225–9236, https://doi.org/10.5194/acp-10-9225-2010, 2010.

Kovilakam, M., Thomason, L. W., Ernest, N., Rieger, L., Bourassa, A., and Millán, L.: The Global Space-based Stratospheric Aerosol Climatology (version 2.0): 1979–2018, Earth Syst. Sci. Data, 12, 2607–2634, https://doi.org/10.5194/essd-12-2607-2020, 2020.

Kyrölä, E., Sihvola, E., Kotivuori, Y., Tikka, M., Tuomi, T., and Haario, H.: Inverse Theory for Occultation Measurements, 1: Spectral Inversion, J. Geophys. Res., 98, 7367–7381, 1993.

Kyrölä, E., Tamminen, J., Sofieva, V., Bertaux, J. L., Hauchecorne, A., Dalaudier, F., Fussen, D., Vanhellemont, F., Fanton d'Andon, O., Barrot, G., Guirlet, M., Mangin, A., Blanot, L., Fehr, T., Saavedra de Miguel, L., and Fraisse, R.: Retrieval of atmospheric parameters from GOMOS data, Atmos. Chem. Phys., 10, 11881–11903, https://doi.org/10.5194/acp-10-11881-2010, 2010.

Malinina, E., Rozanov, A., Rozanov, V., Liebing, P., Bovensmann, H., and Burrows, J. P.: Aerosol particle size distribution in the stratosphere retrieved from SCIAMACHY limb measurements, Atmos. Meas. Tech., 11, 2085–2100, https://doi.org/10.5194/amt-11-2085-2018, 2018.

Malinina, E., Rozanov, A., Rieger, L., Bourassa, A., Bovensmann, H., Burrows, J. P., and Degenstein, D.: Stratospheric aerosol characteristics from space-borne observations: extinction coefficient and Ångström exponent, Atmos. Meas. Tech., 12, 3485–3502, https://doi.org/10.5194/amt-12-3485-2019, 2019.

Miller, R. G.: The Jackknife–A Review, Biometrika, 61, 1, https://doi.org/10.2307/2334280, 1974.

Pohl, C., Wrana, F., Rozanov, A., Deshler, T., Malinina, E., von Savigny, C., Rieger, L. A., Bourassa, A. E., and Burrows, J. P.: Stratospheric aerosol characteristics from SCIAMACHY limb observations: 2-parameter retrieval, Atmos. Meas. Tech. Discuss. [preprint], https://doi.org/10.5194/amt-2023-156, in review, 2023.

Popp, T., De Leeuw, G., Bingen, C., Brühl, C., Capelle, V., Chedin, A., Clarisse, L., Dubovik, O., Grainger, R., Griesfeller, J., Heckel, A., Kinne, S., Klüser, L., Kosmale, M., Kolmonen, P., Lelli, L., Litvinov, P., Mei, L., North, P., Pinnock, S., Povey, A., Robert, C., Schulz, M., Sogacheva, L., Stebel, K., Stein Zweers, D., Thomas, G., Tilstra, L., Vandenbussche, S., Veefkind, P., Vountas, M., and Xue, Y.: Development, Production and Evaluation of Aerosol Climate Data Records from European Satellite Observations (Aerosol_cci), Remote Sens.-Basel, 8, 421, https://doi.org/10.3390/rs8050421, 2016.

Ramachandran, S. and Jayaraman, A.: Balloon-borne study of the upper tropospheric and stratospheric aerosols over a tropical station in India, Tellus B, 55, 820–836, https://doi.org/10.1034/j.1600-0889.2003.00069.x, 2003.

Rieger, L. A., Bourassa, A. E., and Degenstein, D. A.: Stratospheric aerosol particle size information in Odin-OSIRIS limb scatter spectra, Atmos. Meas. Tech., 7, 507–522, https://doi.org/10.5194/amt-7-507-2014, 2014.

Rieger, L. A., Bourassa, A. E., and Degenstein, D. A.: Merging the OSIRIS and SAGE II stratospheric aerosol records, J. Geophys. Res.-Atmos., 120, 8890–8904, https://doi.org/10.1002/2015JD023133, 2015.

Rieger, L. A., Malinina, E. P., Rozanov, A. V., Burrows, J. P., Bourassa, A. E., and Degenstein, D. A.: A study of the approaches used to retrieve aerosol extinction, as applied to limb observations made by OSIRIS and SCIAMACHY, Atmos. Meas. Tech., 11, 3433–3445, https://doi.org/10.5194/amt-11-3433-2018, 2018.

Robert, C. É., Bingen, C., Vanhellemont, F., Mateshvili, N., Dekemper, E., Tétard, C., Fussen, D., Bourassa, A., and Zehner, C.: AerGOM, an improved algorithm for stratospheric aerosol extinction retrieval from GOMOS observations – Part 2: Intercomparisons, Atmos. Meas. Tech., 9, 4701–4718, https://doi.org/10.5194/amt-9-4701-2016, 2016.

Santer, B. D., Bonfils, C., Painter, J. F., Zelinka, M. D., Mears, C., Solomon, S., Schmidt, G. A., Fyfe, J. C., Cole, J. N. S., Nazarenko, L., Taylor, K. E., and Wentz, F. J.: Volcanic contribution to decadal changes in tropospheric temperature, Nat. Geosci., 7, 185–189, 2014.

Schallock, J., Brühl, C., Bingen, C., Höpfner, M., Rieger, L., and Lelieveld, J.: Reconstructing volcanic radiative forcing since 1990, using a comprehensive emission inventory and spatially resolved sulfur injections from satellite data in a chemistry-climate model, Atmos. Chem. Phys., 23, 1169–1207, https://doi.org/10.5194/acp-23-1169-2023, 2023.

Sofieva, V. F.: FMI-GOMOSaero dataset of aerosol extinction profiles (Version 1), Finnish Meteorological Institute [data set], https://doi.org/10.57707/FMI-B2SHARE.46080A1FCE064E71975EA61C9E839721, 2023.

Sofieva, V. F., Tamminen, J., Haario, H., Kyrölä, E., and Lehtinen, M.: Ozone profile smoothness as a priori information in the inversion of limb measurements, Ann. Geophys., 22, 3411–3420, https://doi.org/10.5194/angeo-22-3411-2004, 2004.

Sofieva, V. F., Kan, V., Dalaudier, F., Kyrölä, E., Tamminen, J., Bertaux, J.-L., Hauchecorne, A., Fussen, D., and Vanhellemont, F.: Influence of scintillation on quality of ozone monitoring by GOMOS, Atmos. Chem. Phys., 9, 9197–9207, https://doi.org/10.5194/acp-9-9197-2009, 2009.

Sofieva, V. F., Ialongo, I., Hakkarainen, J., Kyrölä, E., Tamminen, J., Laine, M., Hubert, D., Hauchecorne, A., Dalaudier, F., Bertaux, J.-L., Fussen, D., Blanot, L., Barrot, G., and Dehn, A.: Improved GOMOS/Envisat ozone retrievals in the upper troposphere and the lower stratosphere, Atmos. Meas. Tech., 10, 231–246, https://doi.org/10.5194/amt-10-231-2017, 2017.

Sofieva, V. F., Rozanov, A., Szelag, M., Burrows, J. P., Retscher, C., Damadeo, R., Degenstein, D., Rieger, L. A., and Bourassa, A.: A Climate Data Record of Stratospheric Aerosols, Earth Syst. Sci. Data Discuss. [preprint], https://doi.org/10.5194/essd-2023-538, in review, 2024.

Solomon, S., Daniel, J. S., Neely, R. R., Vernier, J.-P., Dutton, E. G., and Thomason, L. W.: The Persistently Variable "Background" Stratospheric Aerosol Layer and Global Climate Change, Science , 333, 866–870, https://doi.org/10.1126/science.1206027, 2011.

Tamminen, J.: Validation of nonlinear inverse algorithms with Markov Chain Monte Carlo method, J. Geophys. Res., 109, D19303, https://doi.org/10.1029/2004JD004927, 2004.

Tamminen, J. and Kyrölä, E.: Bayesian solution for nonlinear and non-Gaussian inverse problems by Markov chain Monte Carlo method, J. Geophys. Res., 106, 14377–14390, https://doi.org/10.1029/2001JD900007, 2001.

Thomason, L. W., Burton, S. P., Luo, B.-P., and Peter, T.: SAGE II measurements of stratospheric aerosol properties at non-volcanic levels, Atmos. Chem. Phys., 8, 983–995, https://doi.org/10.5194/acp-8-983-2008, 2008.

Vanhellemont, F., Fussen, D., Mateshvili, N., Tétard, C., Bingen, C., Dekemper, E., Loodts, N., Kyrölä, E., Sofieva, V., Tamminen, J., Hauchecorne, A., Bertaux, J.-L., Dalaudier, F., Blanot, L., Fanton d'Andon, O., Barrot, G., Guirlet, M., Fehr, T., and Saavedra, L.: Optical extinction by upper tropospheric/stratospheric aerosols and clouds: GOMOS observations for the period 2002–2008, At-

mos. Chem. Phys., 10, 7997–8009, https://doi.org/10.5194/acp-10-7997-2010, 2010.

Vanhellemont, F., Mateshvili, N., Blanot, L., Robert, C. É., Bingen, C., Sofieva, V., Dalaudier, F., Tétard, C., Fussen, D., Dekemper, E., Kyrölä, E., Laine, M., Tamminen, J., and Zehner, C.: AerGOM, an improved algorithm for stratospheric aerosol extinction retrieval from GOMOS observations – Part 1: Algorithm description, Atmos. Meas. Tech., 9, 4687–4700, https://doi.org/10.5194/amt-9-4687-2016, 2016.

Vernier, J.-P., Thomason, L. W., Pommereau, J.-P., Bourassa, A., Pelon, J., Garnier, A., Hauchecorne, A., Blanot, L., Trepte, C., Degenstein, D., and Vargas, F.: Major influence of tropical volcanic eruptions on the stratospheric aerosol layer during the last decade, Geophys. Res. Lett., 38, L12807, https://doi.org/10.1029/2011GL047563, 2011.